Elevated Methionine Flux Drives Pyroptosis Evasion in Persister Cancer Cells

Asmaa El-Kenawi[1,2], Anders Berglund[3], Veronica Estrella[2,4], Yonghong Zhang[5], Min Liu[6], Ryan M. Putney[3], Sean J. Yoder[7], Joseph Johnson[8], Joel Brown[2,9], and Robert Gatenby[2,9,10]

ABSTRACT

Induction of cell death represents a primary goal of most anticancer treatments. Despite the efficacy of such approaches, a small population of "persisters" develop evasion strategies to therapy-induced cell death. While previous studies have identified mechanisms of resistance to apoptosis, the mechanisms by which persisters dampen other forms of cell death, such as pyroptosis, remain to be elucidated. Pyroptosis is a form of inflammatory cell death that involves formation of membrane pores, ion gradient imbalance, water inflow, and membrane rupture. Herein, we investigate mechanisms by which cancer persisters resist pyroptosis, survive, then proliferate in the presence of tyrosine kinase inhibitors (TKI). Lung, prostate, and esophageal cancer persister cells remaining after treatments exhibited several hallmarks indicative of pyroptosis resistance. The inflammatory attributes of persisters included chronic activation of inflammasome, STING, and type I interferons. Comprehensive metabolomic characterization uncovered that TKI-induced pyroptotic persisters display high methionine consumption and excessive taurine production. Elevated methionine flux or exogenous taurine preserved plasma membrane integrity via osmolyte-mediated effects. Increased dependency on methionine flux decreased the level of one carbon metabolism intermediate S-(5′-adenosyl)-L-homocysteine, a determinant of cell methylation capacity. The consequent increase in methylation potential induced DNA hypermethylation of genes regulating metal ion balance and intrinsic immune response. This enabled thwarting TKI resistance by using the hypomethylating agent decitabine. In summary, the evolution of resistance to pyroptosis can occur via a stepwise process of physical acclimation and epigenetic changes without existing or recurrent mutations.

Significance: Methionine enables cancer cells to persist by evading pyroptotic osmotic lysis, which leads to genome-wide hypermethylation that allows persisters to gain proliferative advantages.

Introduction

Deregulated receptor tyrosine kinases (RTK) such as EGFR and HER2 are associated with cancer development, progression, metastasis and resistance to cancer therapy (1–3). Targeting aberrant RTK signaling can be achieved by blocking its activation. This inhibits downstream signaling such as MEK, and/or forces receptor downregulation (4–6). RTK-targeted therapies are used to treat various malignancies such as non–small cell lung cancer (NSCLC) harboring activating mutations of EGFR (7), melanoma (8), squamous cell carcinoma of the head and neck (9), colorectal (10), esophageal (11), and pancreatic cancers (12). While targeting RTK can be initially highly effective, evolution of resistance almost invariably leads to treatment failure and tumor progression. In many cases, resistance is due to a preexisting mutation, such as $EGFR^{T790M}$, that continues to function despite EGFR inhibition. However, up to half of EGFR inhibitor–resistant lung cancers do not have a T790M mutation (13). Furthermore, some RTK-overexpressing malignancies such as esophageal adenocarcinoma (14) or castration-resistant prostate cancer (15, 16) exhibit intrinsic resistance. In such cases, other mechanisms may contribute to evading of therapy induced cell death. These resistance mechanisms usually involve an evolutionary sequence in which a small number of individual cells (termed "persisters" or "drug-tolerant cells") initially survive for an extended period and then, begin proliferating to produce a therapy-resistant population (17–20).

Inhibitors of the RTKs kill malignant cells via multiple mechanisms of cells death (21–24). To persist, the residual cells must adopt evasion strategies to cell death. While several studies focused on identifying resistance circuitries to apoptosis (21, 25), the evasion mechanisms to pyroptotic cell death remain to be discovered. Pyroptosis is an inflammatory type of lytic cell death that involves release of inflammatory cytokines and cellular content. The gasdermin protein family is an essential effector of pyroptosis. To initiate cell death cascades, gasdermins are cleaved by caspases then oligomerize and translocate to the plasma membrane to establish membrane pores (26). In addition to tyrosine kinase inhibitor (TKI), pyroptotic cell death is induced by a wide range of anticancer treatments such as chemotherapy and during inflammation (27–30). Thus, understanding how cancer cells resist pyroptosis will have broad translational applications.

Here, we investigated the dynamics mediating resistance to TKI-induced lytic cell death focusing on two questions: (i) What cellular

[1]Department of Radiation Oncology, H. Lee Moffitt Cancer Center, Tampa, Florida. [2]Cancer Biology and Evolution Program, H. Lee Moffitt Cancer Center, Tampa, Florida. [3]Department of Biostatistics and Bioinformatics, H. Lee Moffitt Cancer Center, Tampa, Florida. [4]Department of Cancer Physiology, H. Lee Moffitt Cancer Center, Tampa, Florida. [5]Biostatistics and Bioinformatics Shared Resource, H. Lee Moffitt Cancer Center, Tampa, Florida. [6]Proteomics and Metabolomics Core Facility, H. Lee Moffitt Cancer Center, Tampa, Florida. [7]Molecular Genomics Core Facility, H. Lee Moffitt Cancer Center, Tampa, Florida. [8]Analytic Microscopy Core Facility, H. Lee Moffitt Cancer Center, Tampa, Florida. [9]Department of Integrated Mathematical Oncology, H. Lee Moffitt Cancer Center, Tampa, Florida. [10]Department of Radiology, H. Lee Moffitt Cancer Center, Tampa, Florida.

Corresponding Authors: Asmaa El-Kenawi, Moffitt Cancer Center, 12902 Magnolia Drive, Tampa, FL 33612. Phone: 813-745-0114; E-mail: asmaa.elkenawi@cancerimmunometabolism.com; and Robert Gatenby, robert.gatenby@moffitt.org

Cancer Res 2023;83:720–34

doi: 10.1158/0008-5472.CAN-22-1002

properties enable survival of rare persister cells following initial exposure to TKI treatment? (ii) What molecular events permit these pyroptotic persisters to transition from quiescence to a proliferative state producing resistant progeny?

We investigate these questions by combining time-lapse imaging of evolving persisters combined with longitudinal DNA/RNA sequencing and metabolomics. We identified novel metabolic resistance mechanisms to TKI-induced pyroptosis. We demonstrate that high methionine flux and taurine protect cancer cells against pyroptotic osmotic lysis. This excessive methionine flux also alters the cell methylation capacity with a subsequent genome-wide hypermethylation and proliferation. Identifying these resistance mechanisms will have the potential to increase TKI efficacy and to reduce cancer relapse.

Materials and Methods

Cell lines

We used the NSCLC A549 (harboring $KRAS^{G12S}$), PC9 (harboring $^{EGFRE746\text{-}A750\ del}$), and the esophageal OE-19 to represent three common pathogenic scenarios for tyrosine kinase dysregulation. OE-19 and OE-33 were purchased from Sigma. PC9 cells (31) were obtained from the Lung Cancer Center of Excellence at H. Lee Moffitt Cancer Center and Research Institute. DU-145 was obtained from the NCI funded Physical Sciences-Oncology Network Bioresource Core Facility at ATCC. Cells were maintained and cultured according to their suggested protocols using RPMI with L-glutamine supplemented with 10% FBS and penicillin-streptomycin (100 units/mL–100 μg/mL). Resistant cell lines were maintained in 2 μmol/L erlotinib-containing medium. Subculturing was performed when cells reached 90% confluency. Parent and resistant cell lines were authenticated by determining short tandem repeat markers. *Mycoplasma* testing was carried out periodically using Moffitt Cancer Genomics Core service.

Flow cytometry

Cancer cells were seeded in 6-well plates and treated with TKIs for 48–72 hours then heat-shocked PKH26 (Sigma-Aldrich) labeled cells (32) were added for additional 4 hours. Floating cells were discarded and remaining cells were washed with PBS, collected and stained with Calcein Blue, AM. PC9 and resistant cells were then processed for flow cytometry. Calcein Blue, AM permeates live cells where it undergoes esterase-dependent cleavage of their acetoxymethyl (AM) ester group, yielding a membrane-impermeable Calcein Blue fluorescent dye. Pyroptotic, apoptotic and dead cells with compromised cell membranes do not retain Calcein Blue. For oxidative stress, cells were stained with CM-H2DFDA (5 μmol/L) for 15 minutes at 37°C, washed twice then processed for flow cytometry using staining buffer (PBS, 2% BSA) containing DAPI. Data were recorded on a LSR II Flow Cytometer (BD Biosciences) and analysis completed using FlowJo software.

qRT-PCR and NanoString profiling

TaqMan Mutation Detection Assays powered by competitive allele-specific TaqMan PCR (castPCR Technology) was used to validate *EGFR* T790M mutation. For gene expression analysis by NanoString nCounter, RNA was extracted using the RNeasy Isolation Kit (Qiagen) then were hybridized to the human immunology Panel according to the manufacturer's protocol (NanoString Technologies). The resulting RCC files containing raw counts were reviewed for quality and normalized in the NanoString nSolver analysis software v3.0, followed by exportation and analysis.

Phosphorylation and protein quantification

Human Phospho-RTK and Proteome Profiler Human Cytokine Array arrays were used for determination of the relative level of tyrosine phosphorylation of human RTKs in cells and cytokines in medium according to manufacturer's instruction.

Confocal immunofluorescence

Cells on chamber slides were washed twice with PBS, fixed with paraformaldehyde solution, 4% in PBS for 20 minutes and permeabilized with 0.1% Triton X-100 for 5 minutes. Cells were washed twice with PBS, blocked with 2% BSA in PBS for 1 hour and subsequently incubated with indicated antibodies at 4°C overnight. Cells were washed three times with PBS and incubated with appropriate fluorescent-labeled secondary antibodies at room temperature for 1 hour. VECTASHIELD Antifade containing DAPI was used as mounting medium. Images were visualized using Leica TCS SP8 laser scanning microscope (Leica Microsystems) and Images were exported in TIF format with LAS X software version 3.1.5 (Leica Microsystems). Mean fluorescence intensity (MFI) analysis was performed on the TIF images with Definiens Tissue Studio version 4.7 (Definiens AG). In the software, the nucleus detection (DAPI channel) and cell shape (Green or Red channel) algorithms were used to segment individual cells within each image. Using this cell segmentation, the MFI for nucleus and cytoplasm were calculated for each cell. The nucleus to cytoplasm intensity ratio was plotted using R studio version 4.0.3 (33). Catalog numbers of key reagents and antibodies are provided in Supplementary Table S1.

Incucyte imaging

Cells were seeded in 96-well plates at a density of 6,000 cells/well in 100 μL final volume. The next day, the medium was changed to 200 μL of drug containing medium as indicated. Phase contrast images were acquired one to three times a day for the duration of treatment. For estimation of live cell number, medium containing Calcein AM (1.25 μg/mL) and HCS NuclearMask Red stain (1:2,000) were added at the final timepoint of the assay then red and green fluorescence images were acquired within 30 minutes. Tailored algorithm was used to quantify the number of double-positive objects in each treatment condition as indicative of live cell number. For determination of plasma membrane permeability, cells were starved for 1 hour in complete methionine/cystine-free medium [cysteine/cystine, methionine, and glutamine-free RPMI (MP Biomedicals) supplemented with 5% dialyzed FBS, 2 mmol/L glutamine and penicillin-streptomycin (100 units/mL–100 μg/mL)]. Medium was then switched to complete methionine/cystine-free medium containing 100 nmol/L SYTOX Green with or without the following: 25 μmol/L taurine ± 5 μmol/L nigericin, 200 μmol/L ATP, or 75 μmol/L ADOX. Plates were imaged every 30 minutes or 1 hour using IncuCyte S3 or SX5 Live-Cell Analysis System (Sartorius). Tailored algorithm was used to quantify SYTOX green fluorescence/cell. The histogram option was used to determine distribution and frequency of green intensity in individual cells. Catalog numbers of key reagents are provided in Supplementary Table S1.

RNA sequencing

RNA extracted from cell lines was quantitated with the Qubit Fluorometer (Thermo Fisher Scientific) and screened for quality on the Agilent TapeStation 4200 (Agilent Technologies). The samples were then processed for RNA sequencing using the NuGEN Universal RNA-Seq Library Preparation Kit with NuQuant (NuGEN Technologies). Briefly, 50 ng of RNA was used to generate cDNA and a strand-

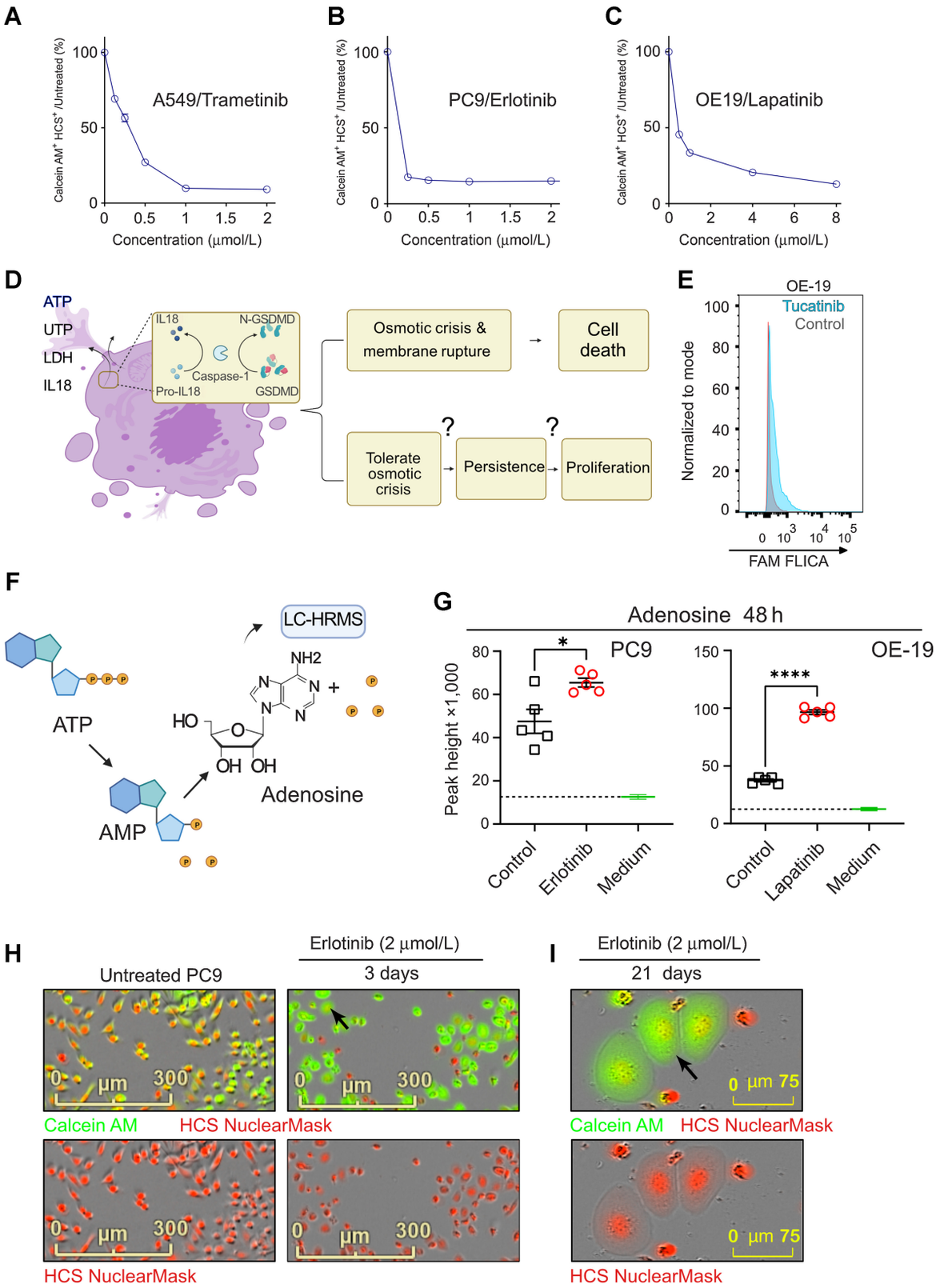
A
A549/Trametinib
Calcein AM+ HCS+ /Untreated (%)
Concentration (μmol/L)
B
PC9/Erlotinib
C
OE19/Lapatinib
D
ATP
UTP
LDH
IL18
IL18
N-GSDMD
Caspase-1
Pro-IL18
GSDMD
Osmotic crisis & membrane rupture
Cell death
Tolerate osmotic crisis
Persistence
Proliferation
E
OE-19
Tucatinib
Control
Normalized to mode
FAM FLICA
F
LC-HRMS
ATP
AMP
Adenosine
G
Adenosine 48 h
PC9
OE-19
Peak height ×1,000
Control
Erlotinib
Medium
Lapatinib
H
Untreated PC9
Erlotinib (2 μmol/L)
3 days
Calcein AM
HCS NuclearMask
I
Erlotinib (2 μmol/L)
21 days

specific library following the manufacturer's protocol. Quality control steps were performed, including TapeStation size assessment and quantification using the Kapa Library Quantification Kit (Roche). The final libraries were normalized, denatured, and sequenced on the Illumina NextSeq 2000 sequencer with the P3-200 cycle reagent kit to generate approximately 80–108 million base read pairs per sample (Illumina, Inc.).

Whole-exome sequencing

Whole-exome sequencing was performed to identify somatic mutations in the coding regions of the human genome. Following a quantitative PCR–based DNA quality and quantity assessment using the Agilent NGS FFPE QC Kit, 200 ng of DNA was used as input into the Agilent SureSelect XT Clinical Research Exome kit, which includes the exon targets of Agilent's v5 whole-exome kit, with increased coverage at 5,000 disease-associated targets (Agilent Technologies). Briefly, for each tumor DNA sample, a genomic DNA library was constructed according to the manufacturer's protocol and the size and quality of the library was evaluated using the Agilent BioAnalyzer. An equimolar amount of library DNA was used for a whole-exome enrichment using the Agilent capture baits and after quantitative PCR library quantitation and QC analysis on the BioAnalyzer, approximately 100 million 75-base paired-end sequences per sample were generated using v2 chemistry on an Illumina NextSeq 500 sequencer (Illumina, Inc.).

MethylationEPIC

A total of 500 ng of extracted and Qubit quantitated DNA was bisulfite converted using Zymo EZ DNA Methylation Kits (Zymo Research) and the converted DNA was used to process and hybridize the Illumina MethylationEPIC BeadChip according to the manufacturer's protocol (Illumina, Inc.). The single-base extension and staining were performed using the Tecan Evo liquid handling system with the Te-Flow (GenePaint) chamber. The arrays were then scanned on an Illumina iScan scanner, and QC was performed using the Illumina GenomeStudio software.

Quantification of amino acid consumption and release

Cells were seeded in 12-well plates then treated on the next day with the indicated drugs in 5% dialyzed phenol red–free DMEM for 72 hours. On day 3, 6.6 μL of labeled amino acid mix with 97% to 99% enrichment for each amino acid (MSK-A2-1.2, stock concentration 2.5 mmol/L for each amino acid except L-cystine, 1.25 mmol/L) was added to each well and cells were allowed to equilibrate at 37°C. Cell-free medium were processed similarly as a negative control. A total of 10 μL aliquots of medium were then aspirated from each well 3 and 6 hours later, quickly frozen on dry ice and kept at −80°C until processing via LC/MS to determine abundance of each ^{12}C and ^{13}C amino acid normalized to cell-free medium.

Targeted LC/MS quantification of amino acids

For reagents, ammonium hydroxide and ammonium carbonate were obtained from MilliporeSigma. LC/MS grade solvents, including water, methanol and acetonitrile, were purchased from Burdick and Jackson, Honeywell, Muskegon, MI (sourced through VWR). For sample preparation, 10 μL of culture medium was collected at the indicated timepoint then 40 μL of 100% −80°C cold methanol was added to each sample to obtain sample in 80% methanol. All processes were carried out on ice. The samples were then vortexed and centrifuged at 18,800 × *g* (Microfuge 22R, Beckman Coulter) at 0°C for 10 minutes. Then, the samples were incubated for 30 minutes in a −80°C freezer to increase metabolite extraction. Another step of centrifugation was performed followed by transferring 20 μL supernatant to autosamples tubes. Ultra-high performance liquid chromatography (UHPLC)-high-resolution mass spectrometry was then performed using a Vanquish UHPLC interfaced with a Q Exactive HF quadrupole-orbital ion trap mass spectrometer (Thermo Fisher Scientific). Chromatographic separation was performed using a SeQuant ZIC-pHILIC guard column (2.1 mm ID × 20 mm length, 5 μm particle size) and a SeQuant ZIC-pHILIC LC column (2.1 mm ID × 150 mm length, 5 μm particle size, MilliporeSigma). Mobile phase A was aqueous 10 mmol/L ammonium carbonate and 0.05% ammonium hydroxide, and mobile phase B was 100% acetonitrile. The gradient program included the following steps: start at 80% B, a linear gradient from 80% to 20% B over 13 minutes, stay at 20% B for 2 minutes, return to 80% B in 0.1 minutes, and re-equilibration for 4.9 minutes for a total run time of 20 minutes. The flow rate was set to 0.250 mL/minute. The autosampler was cooled to 5°C and the column temperature was set to 30°C. Sample injection volume was 5 μL. Full MS with polarity switching was performed from m/z 65 to m/z 900. The Quan Browser, included in the Xcalibur software, was used to determine the concentration of amino acids and adenosine in media. Catalog numbers of additional key reagents are provided in Supplementary Table S1.

Data and materials availability

The RNA sequencing and whole-exome sequencing generated in this study are publicly available in Gene Expression Omnibus at GSE219044 and in NCBI BioProject at PRJNA907280, respectively. All materials, other data, and detailed protocols described in the article will be made available upon request.

Figure 1.

Cancer persister cells exhibit hallmarks of pyroptosis resistance. **A–C,** The NSCLC A549 (harboring $KRAS^{G12S}$), PC9 (harboring $^{EGFRE746\text{-}A750\ del}$), and the esophageal $HER2^{hi}$ OE-19 were treated for 96 hours with genotype-matched treatments: trametinib (a MEK inhibitor), erlotinib (an EGFR inhibitor), and lapatinib (an EGFR/HER2 inhibitor), respectively. Multicolor fluorescence using Calcein AM and HCS NuclearMask Red enabled cell viability analysis and measurement for total number of cells, respectively. Tailored algorithms were used to quantify the number of double-positive objects in each treatment condition. **D,** A diagram representing pore formation and release of cytokines, alarmins, for example, ATP and large molecules, for example, lactate dehydrogenase (LDH) in pyroptosis. **E,** Tucatinib treatment activates caspase-1 quantified using FAM FLICA fluorescence in OE-19 cells. Data represent two biologically independent experiments. Similar results were reproduced using three other cancer cell lines treated with different TKIs. **F,** Stepwise degradation of ATP (very short half-life) into adenosine. **G,** LC/MS measurement of the ATP degradation product, adenosine, in medium of erlotinib-treated PC9 and lapatinib-treated OE-19 and their corresponding controls. Peak height represents a quantitative chromatographic estimation of adenosine abundance. **H** and **I,** Representative images of PC9 cells before and after 3 and 21 days of treatment with 2 μmol/L erlotinib. Imaging with multicolor fluorescence was performed after adding HCS NuclearMask Red and Calcein AM to enable nucleus visualization and assessment of cell viability, respectively. Arrow indicates persister cells remaining following erlotinib treatment with characterized morphology of high cell volume. Data represent two to three biologically independent experiments. Data are presented as mean ± SEM. Student *t* test was utilized for statistical analysis. *, $P < 0.05$; ****, $P < 0.0001$. Images in **H** and **I** are representative of 8 and 12 replicates of three and two independent experiments, respectively. (**D** and **F**, Created with Biorender.com.)

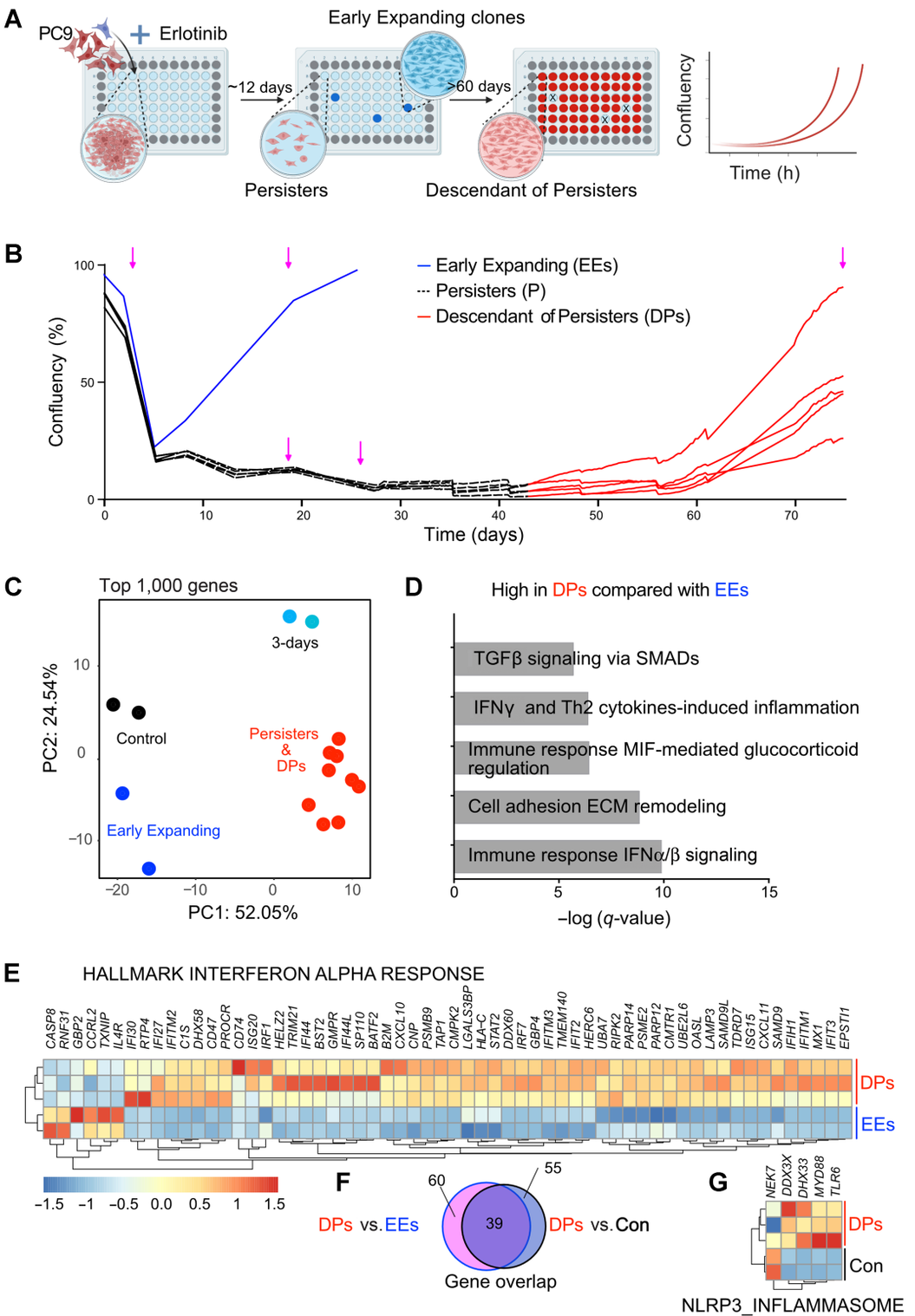

Figure 2.

Pyroptotic persisters display chronic activation of danger-sensing machineries. **A,** Experimental design. PC9 cells were treated in 96-well plate and cells were monitored by Incucyte live-cell imaging. **B,** Independent evolution of EE clones (blue) and DPs (red) after culturing parental PC9 cells in 2 μmol/L erlotinib for the indicated time points. Graph is representative of >3 biologically independent experiments. Arrows, collection time points for RNA/DNA sequencing. **C,** PCA of transcriptome of parental PC9, 3, 19, 27, and 75 days after erlotinib treatment. Day 19 and 27 represent persisters, while day 75 represents DPs. **D,** Pathway analysis of transcriptomic data of DPs compared with EEs. **E** and **F,** Heatmap representing expression of members of HALLMARK INTERFERON ALPHA RESPONSE in DPs versus EEs. Similar results were obtained when we compared expression of DPs versus control with an overlap of 39 genes. **G,** Heatmap representing expression of members of NLRP3 INFLAMMASOME in DPs versus control. (**A**, Created with BioRender.com.)

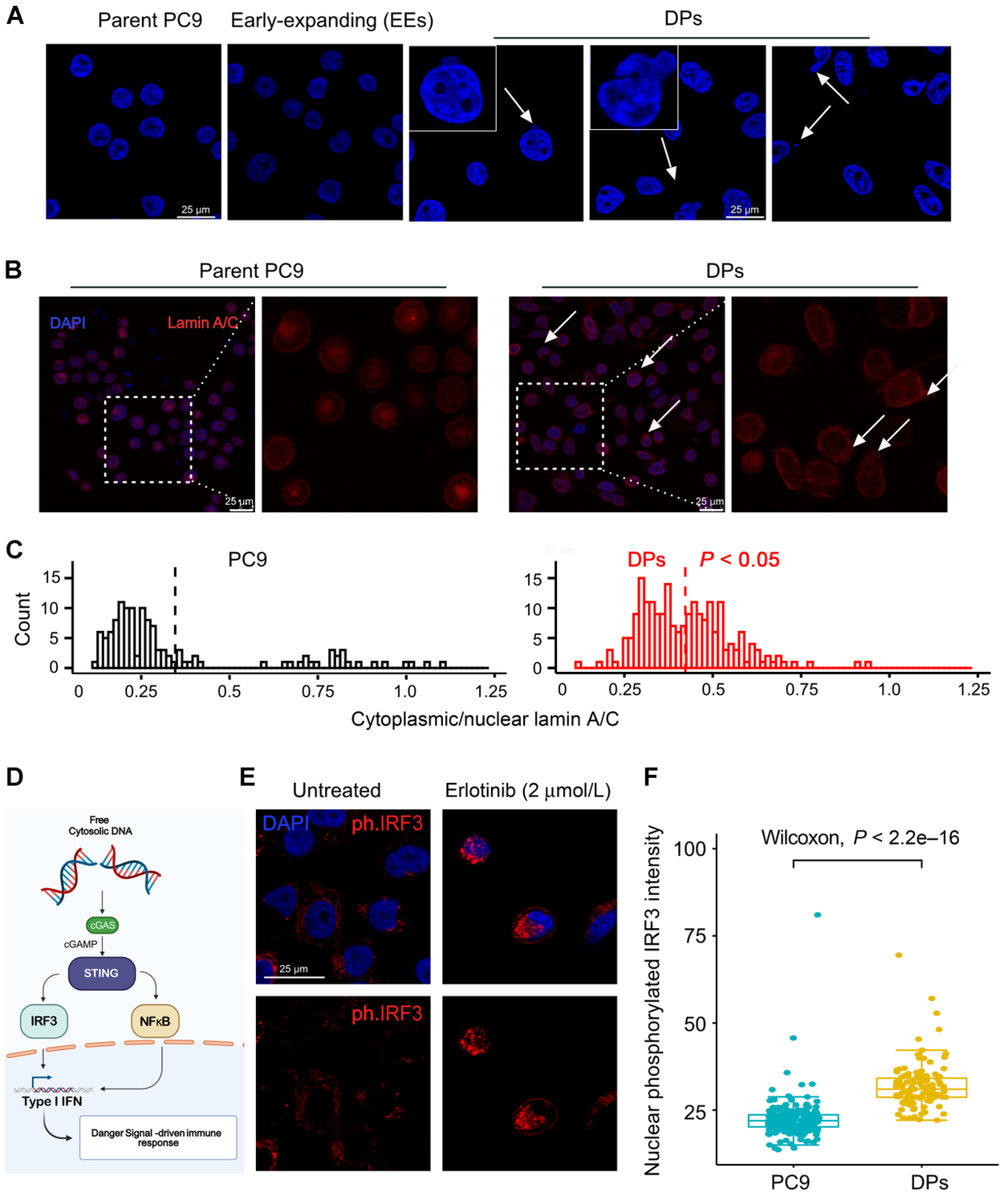

Figure 3.

Pyroptotic persisters exhibit hallmarks of activated cytosolic DNA-sensing machineries. **A,** Confocal microscopy images demonstrating nuclear shape in PC9 cells, EE clones, and different DPs. Arrows, nuclear budding, micronuclei, deformed nuclear shape in DPs. Images represent three fields from one of >3 independent experiments. **B,** Representative confocal microscopy images of DPs and PC9 cells demonstrating disorganization of nuclear lamin A/C (red). DAPI (blue) fluorescence is shown. **C,** The lamin A/C fluorescence intensity for nucleus and cytoplasm compartments was calculated for each cell (339 cells for two conditions), then the cytoplasm/nucleus ratio was computed. Data compiled from six images/condition were then plotted as histograms in R. Figure is a representative of two independent experiments. **D,** Diagram representing how cytosolic DNA can activate type I IFNs via activation of STING and IRF3. **E,** Confocal images representing PC9 cells treated with 2 μmol/L erlotinib for 72 hours then stained with phosphorylated IRF3 antibody showing nuclear localization in erlotinib-treated cells. Figure is representative of three independent experiments. **F,** Quantification of basal nuclear phosphorylated IRF3 in PC9 and DPs. A total of 203 and 115 cells from three images/condition, respectively, were compiled and graphed. Data reflect one of three independent experiments. Wilcox test was utilized for statistical analysis and computed *P* values are displayed. (**D**, Created with BioRender.com.)

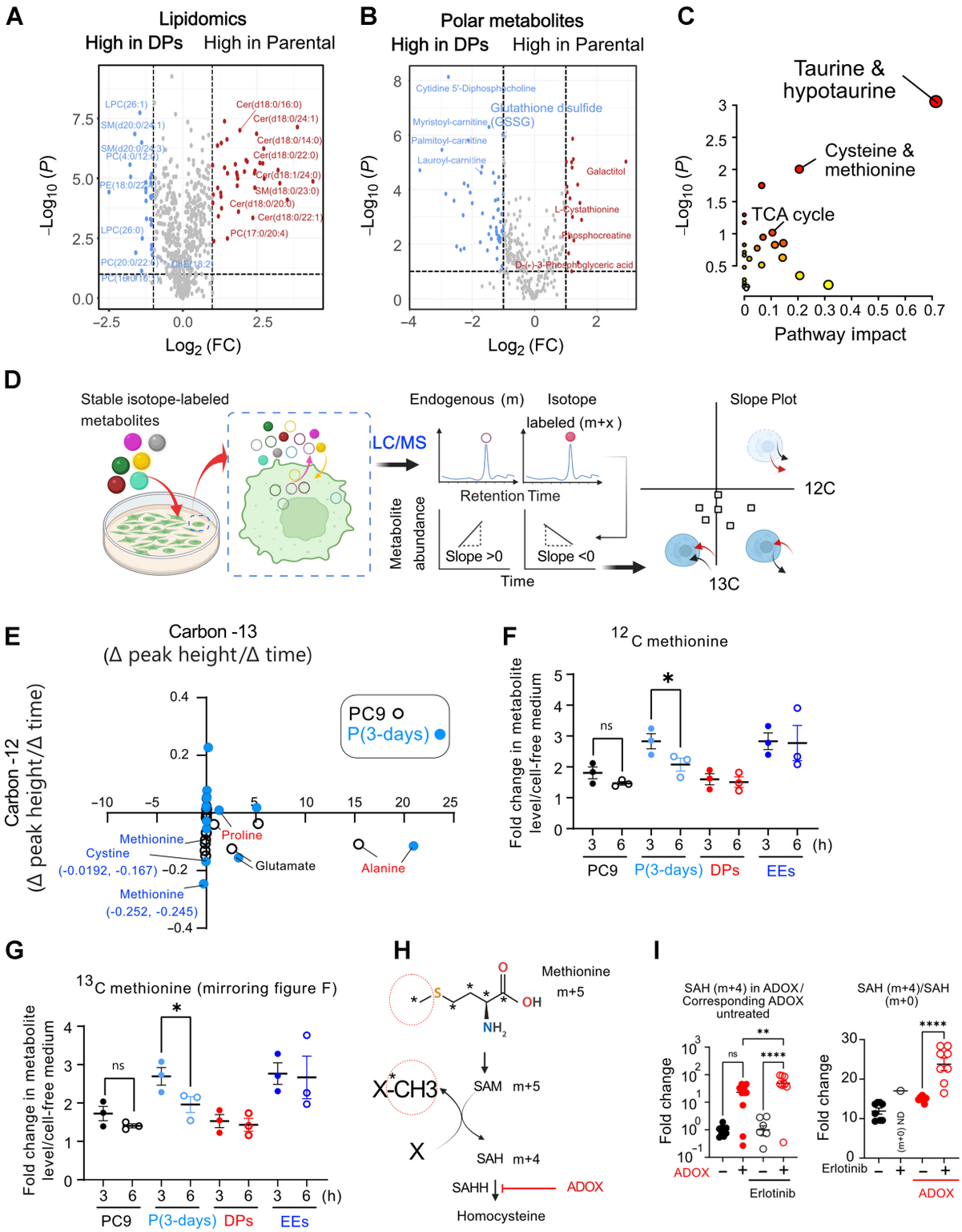

Figure 4.

Persisters display elevated consumption of methionine. **A,** Volcano plot of nonpolar metabolites in DPs and parental cell lines demonstrating high cellular cholesteryl esters in DPs. **B,** Volcano plot of polar metabolites in two different DPs cell lines and parental demonstrating low level of cysteine biosynthesis intermediates, high level of GSSG, and depletion of sugar alcohol galactitol. (*Continued on the following page.*)

Results

Cancer persister cells exhibit hallmarks of pyroptosis resistance

Various TKIs were recently shown to induce cell death via induction of pyroptosis (23, 24). To uncover whether cells can develop resistance to pyroptosis during TKI treatment, we treated A549, PC9 (lung cancer), and OE-19 cells (esophageal cancer) with the genotype-matched treatments: trametinib (MEK inhibitor), erlotinib (EGFR inhibitor), and tucatinib or lapatinib (EGFR/HER2 inhibitors), respectively. We also treated the OE-33 esophageal cancer cells with lapatinib as a control experiment. As expected, these tailored therapies exhibited lethal effects in A549, PC9, and OE-19 cells, respectively, while the $HER2^{low}$ OE-33 cells exhibited intrinsic resistance to lapatinib (**Fig. 1A–C**; Supplementary Fig. S1A). Of note, the esophageal cancer cells OE-19 exhibited high expression of HER2 and displayed a lapatinib-induced decrease in HER2 phosphorylation (Supplementary Fig. S1B and S1C). These treatments induced cell death with balloon-like bubbles reminiscent of pyroptotic cell morphology (23, 24). These morphologic changes result from formation of membrane pores enabling release of cytokines (e.g., IL18) and alarmins (e.g., ATP; refs. 24, 34). In addition, water entering through the pores causes cell swelling, osmotic lysis, and rupturing of the plasma membrane (**Fig. 1D**). Consistent with these hallmarks, tucatinib and/or lapatinib treatment elicited caspase-1 activation and IL18 release in the supernatant of the HER^{hi} OE-19 (**Fig. 1E**; Supplementary Fig. S1D and S1E). Chemotherapy-induced persisters also exhibited chronic activation of caspase-1 (Supplementary Fig. S1F and S1G). Accumulation of extracellular adenosine, a degradation product of ATP, and buildup of lactate dehydrogenase provided further evidence for TKI compromising the plasma membrane integrity (**Fig. 1F** and **G**; Supplementary Fig. S1H). These catastrophic events were observed in most cells, but time-lapse imaging consistently showed a few (∼5%) scattered viable single cells (persisters) remained after 3 days of treatment (**Fig. 1H**). Imaging demonstrated that persister cells underwent swelling, producing a high cell volume (**Fig. 1I**; Supplementary Fig. S1I) in response to the TKI. However, they evade death by deploying an unknown adaptive strategy that prevents plasma membrane rupture.

Pyroptotic persisters display chronic activation of danger-sensing machineries

To better understand mechanism of resistance to pyroptosis during TKI treatment, we focused on PC9, a well-studied, EGFR-addicted NSCLC cell line. As noted, high concentration of erlotinib leaves a small percentage of survivors that enter the persister state (18, 19). For 75 days and under continuous exposure to erlotinib, we used a live imaging protocol to monitor persister cells. This time scale and the small number of cells in each well enabled us to differentiate cells with preexisting mutations, which began proliferating within 12 days of treatment (early expanding, EE) as described previously (18, 19) and drug-tolerant persister cells, which survived TKI-induced osmotic stress but remained viable for about approximately 40 days (persisters, P) before commencing proliferation. Once the "quiescent" persisters (P) began proliferating, we separately investigated the expanding population, which we label "descendants of persisters" (DP; **Fig. 2A** and **B**). DPs were resistant to erlotinib as shown by comparing their IC_{50} with that of the parental PC9 cells (Supplementary Fig. S2A). Interestingly, culturing DPs and EEs in the absence of drug for 52 days did not revert their phenotype to become TKI sensitive (Supplementary Fig. S2B). To dissect the mechanism(s) of resistance to TKI-induced osmotic lysis, we performed DNA/RNA sequencing and metabolomics at different time points during the transition from the P to the DP state (**Fig. 2B**). Whole-exome sequencing and PCR-based detection of point mutations found no additional lung cancer related or *de novo EGFR* mutations in P or their DPs. Specifically, mutations such as *MET, RET*, and *MEK*, known to mediate resistance to TKI (35) were not observed in DPs at day 75 of treatment (Supplementary Fig. S2C). Interestingly, the EE clones were found to harbor T790M mutation as expected (we will refer to them as EE^{T790M}; Supplementary Fig. S2D). Despite being genetically identical, principal component analysis (PCA) of transcriptomic data demonstrated that P and DPs are transcriptionally distinct from the parental cell line (**Fig. 2C**). Pathway analysis illustrates that DPs exhibit a characteristic activation of intrinsic immune circuits including IFNα/β signaling (**Fig. 2D–G**). In support, nCounter profiling of six cell lines from DPs and seven cell lines from EEs demonstrates chronic activation of inflammasome and Toll-like receptors (TLR) danger-sensing machineries in most DPs (Supplementary Fig. S2E–S2G). Identifying the mechanisms by which persisters elicit this intrinsic inflammatory phenotype or adapt to its determinantal effects will enable us to identify novel liabilities of TKI resistance.

Pyroptotic persisters exhibit hallmarks of activated cytosolic DNA-sensing machineries

Activation of type I IFNs is commonly associated with cytosolic DNA. These cytoplasmic polynucleotides originate from viral infection, micronuclei formation associated with mitotic defects, mtDNA release associated with mitochondrial damage or phagocytosis of dead cell corpses (36). Thus, we next examined whether there are increased levels of DNA in the cytosol of DPs. Confocal microscopy in **Fig. 3A**; Supplementary Fig. S3A and S3B illustrates that DPs exhibit large less-round nuclei, frequent nuclear budding and cytoplasmic micronuclei. DPs also display disorganized nuclear lamin A/C with cytoplasmic protrusions (**Fig. 3B** and **C**). Of note, lamin A/C plays an important role in maintaining proper nuclear morphology and protecting against chromosomal numerical instability and aneuploidy (37, 38). To

(*Continued.*) **C,** Metabolic pathway analysis of top differentially abundant polar metabolites indicating perturbation in methionine, cysteine, and taurine metabolism. **A–C,** were generated in MetaboAnalyst**. D,** Determination of amino acid consumption and release profiles using isotope-labeled metabolites. PC9 cells were treated with erlotinib for 72 hours, then mixture of isotopically labeled amino acid was spiked into the medium. Aliquots of the culture media were collected 3 and 6 hours later and processed by LC/MS. **E,** Plot of ^{13}C and ^{12}C slope representing 3 hours change in normalized abundance of isotopically labeled and endogenous amino acids, respectively. Data reflect one of two independent experiments. **F** and **G,** A 3 hours fold change of normalized abundance of isotopically labeled ^{13}C and ^{12}C methionine in PC9, PC9 treated with erlotinib, EEs, and DPs. **H,** Conversion of methionine (m+5) to SAM (m+5). SAM-mediated methylation of substrates results in losing a labeled carbon from SAM to produce the labeled mass isotopomer m+4 of SAH. ADOX interrupts the methionine flux by inhibiting S-adenosyl-L-homocysteine hydrolase, leading to accumulation of SAH if there is high flux. **I,** PC9 cells were treated with 2 μmol/L erlotinib using complete methionine/cystine-free medium supplemented with 200 μmol/L $^{13}C_5$-methionine and 200 μmol/L cystine at (time zero). After 44 hours, ADOX was added to a set of untreated and TKI-treated cells for additional 4 hours. Levels of $^{13}C_4$-SAH (m+4) and SAH (m+0) in each condition were examined. Graph demonstrates that ADOX increased SAH (m+4) and SAH (m+4)/SAH (m+0) ratio in erlotinib-treated cells. ND, no detection, and it is mostly for SAH (m+0) in $erlotinib^+$ $ADOX^-$ condition. Data are shown as mean ± SEM of three independent experiments compiled ($n = 9$). Student t test was utilized for statistical analysis. *, $P < 0.05$; **, $P < 0.01$; ****, $P < 0.0001$; ns, nonsignificant. (**D**, Created with BioRender.com and Affinity.)

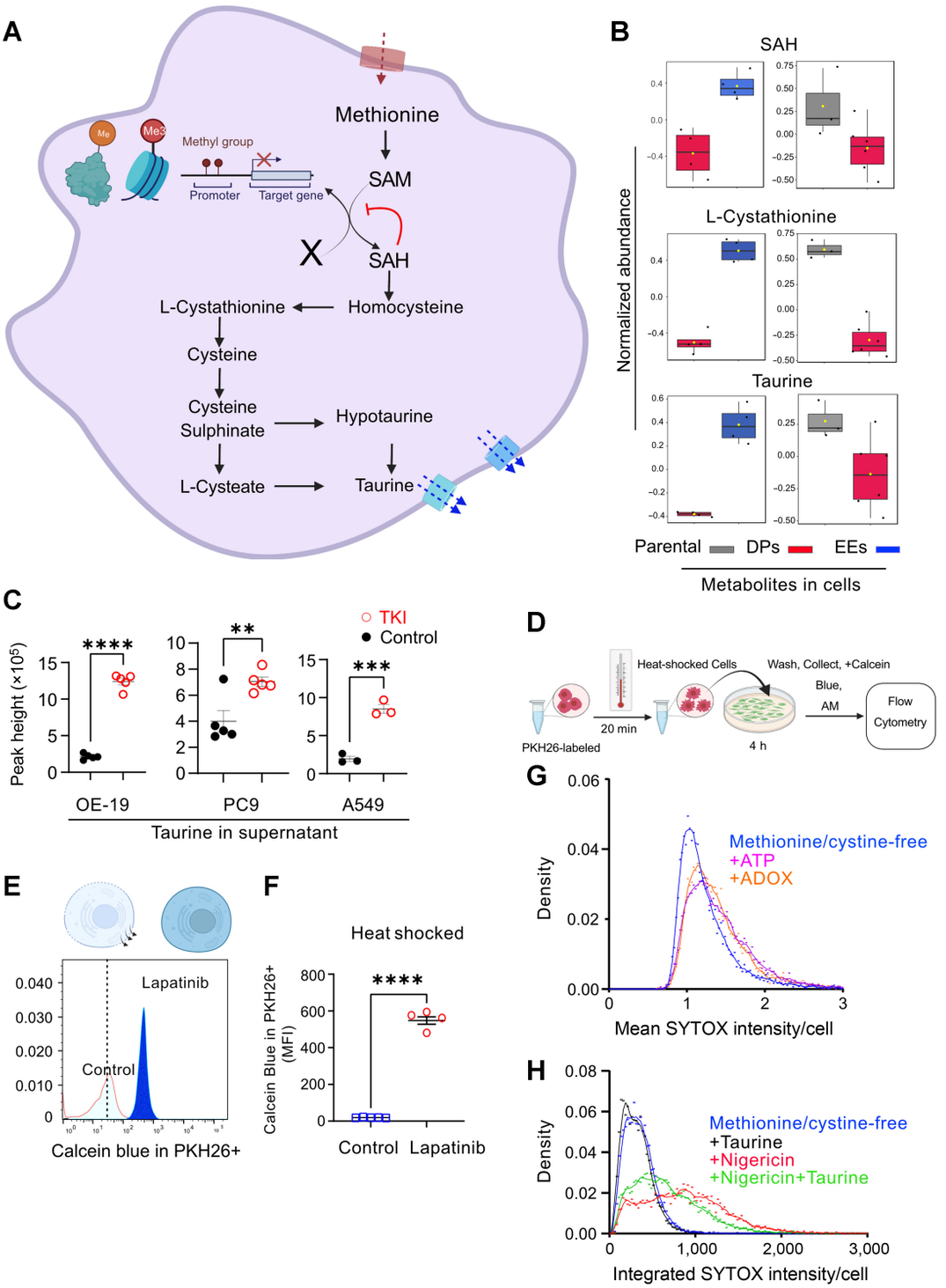

Figure 5.

Organic osmolytes maintain plasma membrane integrity and counteract osmotic crisis. **A,** Diagram representing the flux of methionine into taurine and anticipated hypermethylation of cellular substrates. X, a substrate for a methylation reaction. **B,** Normalized metabolite abundance of SAH, L-cystathionine and taurine in DPs compared with EEs or parental. Data reflect one of three and two independent experiments, respectively. Significance determined by two-way ANOVA and metabolites of interest with FDR < 0.05 are shown. **C,** Normalized metabolite abundance of taurine in medium from the NSCLC A549 (harboring $KRAS^{G12S}$), PC9 (harboring $^{EGFRE746\text{-}A750\ del}$), and the esophageal $HER2^{hi}$ OE-19 treated with TKI or left untreated as control. **D,** OE-19 or PC9 cells were labeled with the lipophilic dye PKH26 then heat shocked at 60°C for 20 minutes. (*Continued on the following page.*)

further ascertain genomic instability, we examined the exacerbated DNA damage in DPs versus EEs and parental PC9 cells in response to genotoxic agents using phosphorylated γH2AX as a surrogate. Following 3 hours exposure to cisplatin, DPs had a higher increase in phosphorylated γH2AX than EEs or parental cells (Supplementary Fig. S3C and S3D). In addition, three different DPs cell lines were more sensitive to the cytotoxic effect of cisplatin than parental PC9 cells (Supplementary Fig. S3E). These signs may suggest replication stress as a major cause of genome instability (39). However, more studies are in need to further investigate the link between replication stress and persistence. Once in the cytosol, these polynucleotides can induce type I IFNs via a cascade of events that eventually triggers phosphorylation of IFN regulatory factor 3 (IRF3; refs. 40, 41). Thus, we then examined translocation of phosphorylated IRF3 in DPs and the parental PC9 cells as a surrogate of chronic intrinsic cyclic GMP–AMP synthase (cGAS)-stimulator of interferon genes (STING) activation (**Fig. 3D**). As we expected, erlotinib caused phosphorylated IRF3 to translocate to the nucleus (**Fig. 3E**). Interestingly, we found that the nuclear level of phosphorylated IRF3 is higher in DPs than in parental PC9 cells (**Fig. 3F**). Collectively, these findings suggest that DPs chronically activate cytosolic DNA-sensing machineries.

Persisters display elevated consumption of methionine

Previous studies demonstrated that cells adopt opposing machineries to dampen danger signals sensing during pyroptosis (42, 43). These counteractive mechanisms include gasdermin E (GSDME) epigenetic silencing through methylation (42) and efflux of K^+ ions via gasdermin D (GSDMD)-mediated membrane pores limiting cGAS-driven type I IFNs (43). The metabolic determinants of resistance to pyroptosis are not fully characterized. A pioneer study unraveled that the tricarboxylic acid cycle intermediate fumarate halts pyroptotic cascade. Fumarate functions by converting the cysteines in GSDMD to S-(2-succinyl)-cysteines. This inhibits caspase-dependent cleavage of GSDMD, pore formation as well as osmotic crisis (44). To dissect the role of metabolism, we then employed a comprehensive metabolomic approach to identify novel mediators that can dampen the detrimental TKI-induced stress responses. Untargeted metabolomics of polar metabolites and lipids demonstrate that DPs and EE^{T790M} are metabolically distinct, (Supplementary Fig. S4A and S4B). In support with previous findings (44), we found increased level of fumarate and succinate in DPs (Supplementary Fig. S4C). We also observed depletion of various dihydroceramides such as Cer(d18:0/16:0) in DPs (**Fig. 4A**). Compared with ceramides, dihydroceramides are saturated structural sphingolipids that tend to decrease plasma membrane fluidity (45). The DPs' metabolic phenotype is also characterized by high intracellular levels of lipids such as triglycerides and cholesteryl esters (**Fig. 4A**; Supplementary Fig. S4D). This could result from *de novo* lipid biosynthesis or scavenging extrinsic lipids (33). *De novo* lipogenic programs were shown to mediate EGFR oncogenic signaling and TKI-acquired resistance (46, 47). In fact, mutated EGFR in TKI-resistant tumor cells relies on EGFR palmitoylation, a process in which palmitate, synthesized *de novo*, is attached to EGFR (48). In addition to *de novo* synthesis of lipids, we found a global depletion of lipids such phosphatidylethanolamines in the media of DPs compared with media from parental PC9 and EE^{T790M} cultures, suggesting high activity of lipid scavenging (Supplementary Fig. S4E). This is also consistent with transcriptomic data demonstrating high expression of fatty acid transporters such as SLC27A4 (49, 50). The DPs also exhibited high intracellular levels of acylcarnitines, such as myristoyl-L-carnitine and palmitoyl-L-carnitine (**Fig. 4B**), and high expression of SLC25A20, which transports acylcarnitines into mitochondrial matrix (51). Despite high level of acylcarnitines, etomoxir, an irreversible inhibitor of carnitine palmitoyltransferase-1, had minimal impact on oxygen consumption rate in DPs (Supplementary Fig. S4F). Instead, blocking pyruvate from entering the mitochondria using UK5099 significantly abrogated oxygen consumption in parental and resistant clones DPs and EEs. Furthermore, BPTES, an allosteric glutaminase (GLS1) inhibitor, reduced oxygen consumption in DPs and EEs but not in parental (Supplementary Fig. S4F). This indicates an important role of glutamine in energy production in DPs and EEs, which may be needed to supplement their high basal oxygen demand (Supplementary Fig. S4F). Further mining of the polar metabolome demonstrates depletion of methionine and cysteine metabolism intermediates in DPs compared with parental PC9 or EE^{T790M} cells (**Fig. 4B**; Supplementary Fig. S4G). In support, pathway analysis of these metabolomic data revealed significant alterations in methionine, cysteine, and taurine metabolism (**Fig. 4C**; ref. 20). This could be due to defective plasma membrane transport or excessive flux of methionine to produce metabolic end products. To investigate this, we developed a fluxomics technique to simultaneously examine production and consumption rates of a panel of amino acids (**Fig. 4D**). This approach confirmed the preferential consumption of methionine in erlotinib-treated cells (**Fig. 4E–G**). To further confirm increased flux, we treated cells with TKI in presence of ADOX, which interrupts the methionine flux by inhibiting S-adenosyl-L-homocysteine hydrolase, leading to accumulation of S-(5′-adenosyl)-L-homocysteine (SAH). We expected that high flux of methionine leads to accumulation of more fraction of the downstream metabolite SAH (m+4) in ADOX treated. Thus, we treated PC9 cells with erlotinib using medium containing $^{13}C_5$ methionine at (time zero). After 44 hours, we added ADOX to a set of untreated and TKI-treated cells for additional 4 hours. We examined the level of $^{13}C_4$-SAH (m+4) and SAH (m+0) in each condition with (m+0) represents residual SAH synthesized before time zero. **Figure 4H** and **I** demonstrate that adding ADOX for the last 4 hours before collection increased SAH (m+4) and SAH (m+4)/SAH (m+0) ratio in erlotinib-treated cells validating increased flux of methionine during persistence. While high methionine flux may be required to combat oxidative stress evident by high level of GSSG (Supplementary Fig. S4B) and high reactive oxygen species (ROS) in persisters (Supplementary Fig. S4H), elucidation of additional novel mechanisms holds a promise in delaying therapy resistance to TKI.

(*Continued.*) Heat-shocked cells were then added to TKI-treated cells or their corresponding control for 4 hours. Attached cells were then washed and processed for flow cytometry in the presence of Calcein Blue, AM. **E** and **F,** Increase in the retention of Calcein Blue in PKH26-labeled/heat-shocked cells incubated with lapatinib-treated OE-19 or erlotinib-treated PC9 cells. Data reflect one of two to three independent experiments. Data are presented as mean ± SEM. **G,** PC9 cells were starved in complete methionine/cystine-free medium for 1 hour, then cells were treated with 75 μmol/L ADOX or 200 μmol/L ATP in complete methionine/cystine-free medium containing 100 nmol/L SYTOX. Cells were imaged at 4 hours using Incucyte. Histograms represent distribution of SYTOX staining/cell as indirect measurement of plasma membrane permeability. **H,** PC9 cells were also starved in complete methionine/cystine-free medium for 1 hour, then cells were treated with 5 μmol/L nigericin with or without 25 μmol/L taurine in complete methionine/cystine-free medium containing 100 nmol/L SYTOX. Histograms represent distribution of SYTOX staining as indirect measurement of plasma membrane permeability at 90 minutes. Data were compiled from >8 images/condition and reflect one of at least four independent experiments. Student *t* test was utilized for statistical analysis. **, $P < 0.01$; ***, $P < 0.001$; ****, $P < 0.0001$. (**A** and **D**, Created with BioRender.com.)

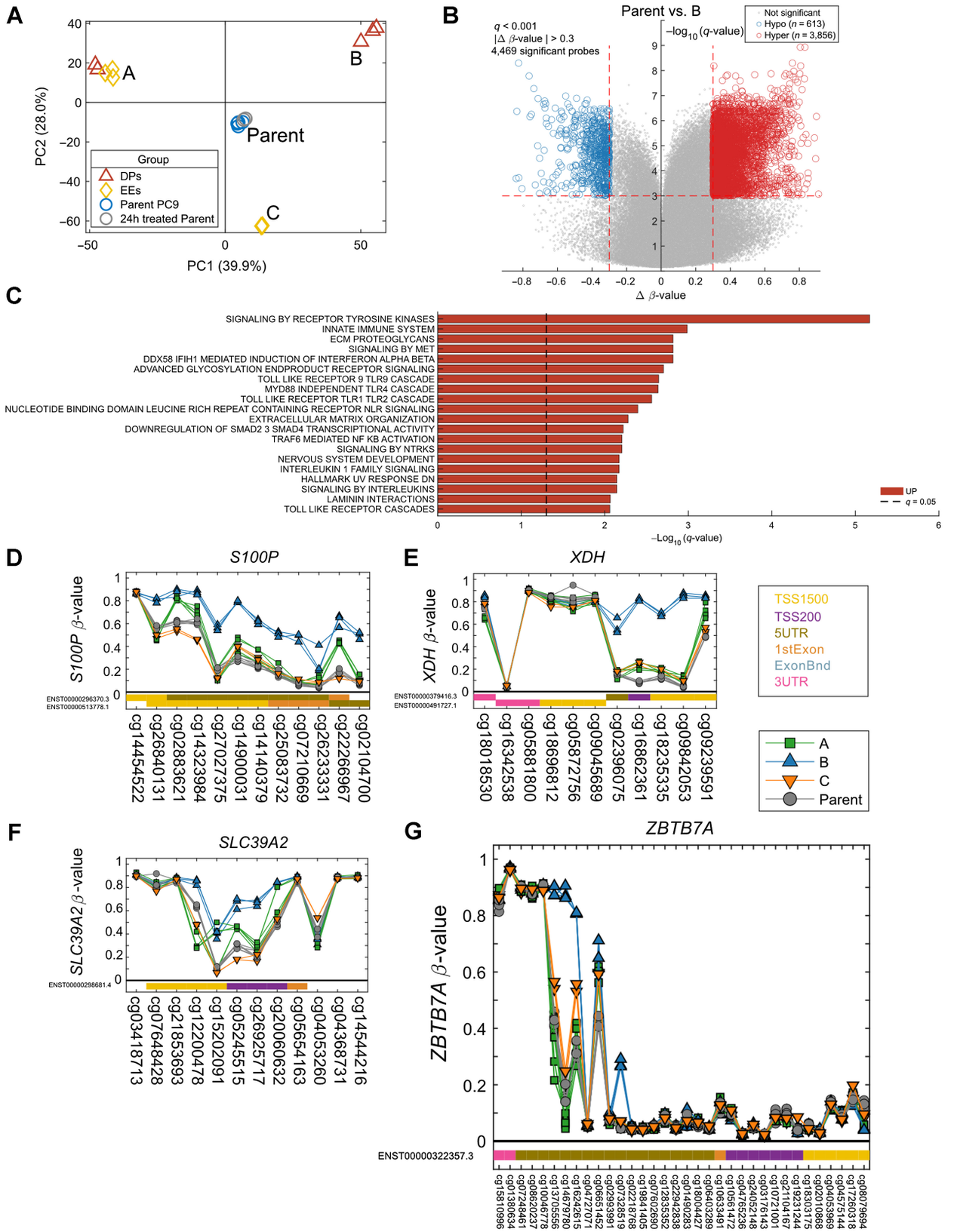
A
PC2 (28.0%)
PC1 (39.9%)
Group
DPs
EEs
Parent PC9
24h treated Parent
B
Parent vs. B
q < 0.001
|Δ β-value | > 0.3
4,469 significant probes
Not significant
Hypo (n = 613)
Hyper (n = 3,856)
Δ β-value
C
SIGNALING BY RECEPTOR TYROSINE KINASES
INNATE IMMUNE SYSTEM
ECM PROTEOGLYCANS
SIGNALING BY MET
DDX58 IFIH1 MEDIATED INDUCTION OF INTERFERON ALPHA BETA
ADVANCED GLYCOSYLATION ENDPRODUCT RECEPTOR SIGNALING
TOLL LIKE RECEPTOR 9 TLR9 CASCADE
MYD88 INDEPENDENT TLR4 CASCADE
TOLL LIKE RECEPTOR TLR1 TLR2 CASCADE
NUCLEOTIDE BINDING DOMAIN LEUCINE RICH REPEAT CONTAINING RECEPTOR NLR SIGNALING
EXTRACELLULAR MATRIX ORGANIZATION
DOWNREGULATION OF SMAD2 3 SMAD4 TRANSCRIPTIONAL ACTIVITY
TRAF6 MEDIATED NF KB ACTIVATION
SIGNALING BY NTRKS
NERVOUS SYSTEM DEVELOPMENT
INTERLEUKIN 1 FAMILY SIGNALING
HALLMARK UV RESPONSE DN
SIGNALING BY INTERLEUKINS
LAMININ INTERACTIONS
TOLL LIKE RECEPTOR CASCADES
UP
q = 0.05
−Log10 (q-value)
D
S100P
S100P β-value
ENST00000296370.3
ENST00000513778.1
cg14454522
cg26840131
cg02883621
cg14323984
cg27027375
cg14900031
cg14140379
cg25083732
cg07210669
cg26233331
cg22266967
cg02104700
E
XDH
XDH β-value
ENST00000379416.3
ENST00000491727.1
cg18018530
cg16342538
cg05881800
cg18696812
cg05872756
cg09045689
cg02396075
cg16862361
cg18235335
cg09842053
cg09239591
TSS1500
TSS200
5UTR
1stExon
ExonBnd
3UTR
A
B
C
Parent
F
SLC39A2
SLC39A2 β-value
ENST00000298681.4
cg03418713
cg07648428
cg21853693
cg12200478
cg15202091
cg05245515
cg26925717
cg20060632
cg05654163
cg04053260
cg04368731
cg14544216
G
ZBTB7A
ZBTB7A β-value
ENST00000322357.3
cg15810996
cg01380634
cg07248461
cg08620237
cg10046778
cg13705556
cg14679780
cg16242615
cg04727071
cg06651452
cg02983991
cg07328519
cg02218768
cg19841405
cg07602690
cg12835352
cg22942838
cg01490283
cg18004427
cg06403289
cg10633491
cg10561472
cg24765236
cg24052148
cg03176143
cg10721001
cg21104167
cg19231244
cg18303175
cg02010868
cg04053969
cg04575144
cg17260318
cg08079694

Organic osmolytes maintain plasma membrane integrity and counteract osmotic crisis

Because excessive methionine flux is observed within 72 hours of treatment (**Fig. 4E**), we reasoned that methionine-dependent strategies contribute to the survival of P cells during the osmotic stress phase (**Fig. 1D**). Besides increasing methylation capacity and combating oxidative stress, high methionine consumption may indicate metabolic dependency on the products of cysteine metabolism: hypotaurine and taurine (**Fig. 5A**). Thus, we hypothesized that these amino acids could function as organic osmolytes to preserve cell volume. Organic osmolytes such as amino acids (e.g., taurine, betaine, alanine, and proline) or sugar alcohols (e.g., galactitol) are compounds released during hypoosmotic cell swelling (52). During hypoosmotic swelling, the net efflux of osmolytes triggers exit of obligated water and regulatory volume decrease (53). In such case, release of these compounds would counteract the TKI-induced osmotic dynamics that otherwise would result in cell death from membrane rupture (**Fig. 1D**; ref. 54). Consistent with this hypothesis, we found that intracellular levels of organic osmolytes such as taurine and galactitol were significantly lower in DPs compared with parental and EEs (**Figs. 5B** and **4B**). This results from continuous pumping of these metabolites outside the cells as suggested by high level of taurine, alanine, and proline in extracellular medium when different cells were treated with the corresponding TKI (**Figs. 5C** and **4E**).

We then examined the role of osmolyte-producing phenotype in maintaining plasma membrane integrity during TKI-induced cell persistence. OE-19 and PC9 cells were labeled with the lipophilic dye PKH26 and then heat shocked at 60°C for 20 minutes (32). Heat-shocked cells were cocultured with their corresponding TKI-treated or untreated cell lines for 4 hours in the presence of Calcein Blue, AM or SYTOX Green (**Fig. 5D**; Supplementary Fig. S5A and S5B). Calcein Blue AM permeates live cells where it undergoes esterase-dependent cleavage of their AM ester group, yielding a membrane-impermeable Calcein Blue fluorescent dye. Pyroptotic, apoptotic and dead cells with compromised cell membranes do not retain Calcein Blue. SYTOX Green is a green fluorescent nuclear and chromosome counterstain, which permeate cells with compromised plasma membrane integrity. These stains enabled us to examine the integrity of plasma membrane in $PKH26^+$ as heat shock perturbs plasma membrane. Using such experimental design, we observed an increase in Calcein Blue retention in $PKH26^+$ cells when incubated with TKI-treated cells (**Fig. 5E** and **F**; Supplementary Fig. S5A). These data suggest that extracellular factors stabilized plasma membrane integrity or promoted esterase enzymatic and metabolic activity in heat-shocked $PKH26^+$ cells. To differentiate between these two possibilities, we then examined permeation of the high molecular weight nuclear dye SYTOX by confocal microscopy following by image analysis to subset heat-shocked $PKH26^+$ cells (Supplementary Fig. S5B–S5D). These experiments indicated low fluorescence of SYTOX green in $PKH26^+$ cells incubated with TKI-treated cells compared with $PKH26^+$ cells incubated with untreated (Supplementary Fig. S5E). To provide more mechanistic insights to the role of methionine flux and organic osmolytes, we then examined permeation of SYTOX when cells were treated with ADOX in methionine/cysteine-deficient medium compared with the pyroptosis-inducing agent ATP as a positive control. Interestingly, ADOX, which interrupts the methionine flux by inhibiting S-adenosyl-L-homocysteine hydrolase, also can induce loss of plasma membrane integrity (**Fig. 5G**). Similarly, nigericin, which activates NLRP3 inflammasome with features of caspase-1–mediated pyroptosis, enhanced SYTOX uptake as a sign of loss of plasma membrane integrity at 90 minutes (**Fig. 5H**). Adding exogenous taurine partially protected against nigericin induced permeabilization of plasma membrane in methionine- and cysteine-deficient medium, (**Fig. 5H**). Collectively, these findings demonstrate that metabolic reprogramming generates an adaptive strategy for TKI-induced cytotoxicity through maintenance of plasma membrane integrity.

Genome-wide DNA hypermethylation regulates osmotic tolerance and proliferation

The methionine cycle also produces the universal methyl donor S-(5′-adenosyl)-L-methionine (SAM), which is crucial for the methylation of many cellular targets such as nucleic acids and proteins. Methylation reaction is regulated by SAH through inhibitory effect on SAM-dependent methyltransferases (55). Notably, DPs have low levels of SAH (**Fig. 5B**) that may impact cell methylation potential. This is further supported by high expression of methyltransferases in DPs (Supplementary Fig. S6A). To investigate whether high methylation capacity in P and DPs results in differential DNA methylation, we performed genome-wide methylation profiling of PC9 cells, 72 hours erlotinib-treated PC9, EE^{T790M}, and DPs. A PCA model using all CpG-probes ($n = 864{,}351$) identified four distinct groups based on PC1 and PC2 (**Fig. 6A**). The first two principal components explained 67.9% of the variation in the data. The parent PC9 and 72 hour–exposed cells exhibited similar DNA methylation patterns. Furthermore, group A consisted of both DPs and EE^{T790M}, while group B consisted of only DPs and group C consisted of only EE^{T790M} (**Fig. 6B**). Statistical analysis followed by volcano plots visualization demonstrates a unique differential DNA hypermethylation when we compared Group B with Parent cells (**Fig. 6C**; Supplementary Fig. S6B and S6C). Pathway-based analysis of top differentially methylated genes in group B DPs found enrichment of IFNα/β, TCRs, and SMADs cascades (**Fig. 6C**; Supplementary Fig. S6D). Surprisingly, we observed that promotor regions of most of these differentially methylated genes encode metal ion (calcium, copper, molybdenum/iron, and zinc) binding proteins, enzymes, and transporters (**Fig. 6D–G**). Querying mRNA expression of genes regulating calcium, iron, zinc ions response/transport supports metal ion imbalance in DPs versus control (Supplementary Fig. S6E). In support, the differentially methylated zinc transporter *SLC39A2*, transcription factors *ZBTB7A* and *ZNF630* exhibited low mRNA expression in DPs (Supplementary Fig. S6F). Of note, zinc balance was shown to regulate inflammatory circuitries associates with pyroptosis such as the NLRP3 inflammasome (56, 57). By limiting zinc availability, pyroptotic persisters can dampen the detrimental effects danger signals sensing. Because of the critical role methylation changes in promoting proliferation, we examined disturbing DPs epigenetics as a therapeutic approach. Consistent with this, we found preferential sensitivity of DPs to the hypomethylating agent decitabine, 5-aza-2′-deoxycytidine (Supplementary Fig. S6G). Collectively, these findings

Figure 6.

Genome-wide DNA hypermethylation regulates osmotic tolerance and proliferation. **A,** A PCA score using all CpG probes with DPs (red triangles), EEs (yellow diamonds), and parents PC9 and 24 hour–treated PC9 (blue and gray circles), respectively. **B,** Volcano plot of *q*-values on the *y*-axis and Δβ-value on the *y*-axis. Dotted redlines, $q < 0.001$ and abs (Δβ-value) >0.3. Red, hypermethylated CpG probes; blue, hypomethylated CpG probes. **C,** Gene set analysis for the significantly differently hypermethylated genes using the REACTOME gene set. Line plots indicating the methylation level for *S100P* (**D**), *XDH* (**E**), *SLC39A2* (**F**), and *ZBTB7A* (**G**) across the different CpG probes for the selected genes with PCA group. A, green boxes; B, blue up-triangles; C, orange down-triangles; parent, gray circles.

demonstrate that metabolism-dependent epigenetic reprograming can contribute to evasion of TKI-induced pyroptotic cell death.

Discussion

Pyroptosis is a critical form of cell death in immunity, inflammation, and cancer initiation (27). In addition, pyroptotic cell death is an emerging determinant of the efficacy of many chemotherapies, radiotherapy, and anticancer molecular targeted agents (23, 24, 27–30). Canonical pyroptotic cell death involves inflammasome assembly followed by cascade of events that result in oligomerization of cleaved gasdermin D to form the permeability pores (34). The assembly of inflammasome is triggered by cytosolic pattern recognition receptors recognizing pathogen-associated molecular patterns (PAMP) and danger-associated molecular patterns and (DAMP; ref. 30). These DAMPs such as ATP are compartmentalized molecules located inside the cell to perform normal physiologic functions (27). However, they can trigger cell damage responses when released outside their compartments or outside the cell (58, 59). Activation of these canonical or other noncanonical pathways leads to osmotic imbalance and cell lysis. The metabolic mechanisms that dampen this important form of cell death are not yet fully understood. A landmark study demonstrated that the tricarboxylic acid cycle intermediate fumarate can halt pyroptotic cascade. Fumarate act by converting the cysteines in GSDMD to S-(2-succinyl)-cysteines, which inhibit caspase-dependent cleavage of GSDMD, pore formation, as well as osmotic crisis (44). In the current study, we uncovered that high methionine to taurine metabolic flux represents a strategy to evade pyroptotic-induced osmotic crisis. Uncovering these mechanisms hold the promise of abrogating the evolution of resistance to anticancer treatments.

Evolution of resistance is a major barrier to prolonged tumor control with targeted therapy. The mechanism of resistance is long thought to be genetically encoded in a small subpopulation of cancer cells (18, 19). However, the higher rate for gaining or losing methylation per CpG site compared with the spontaneous mutation rate per nucleotide base pair per each division underpins nongenetic drivers of resistance (60, 61). In this study, we also investigate how metabolism dependent evolutionary trajectories enable inherited phenotypic changes. When we imposed selection pressures on cancer cells, some gain a short-term survival advantage via excessive acquisition of extracellular nutrients and structural lipids. While this metabolic scavenging phenotype can result from random cellular fluctuations, metabolic state of persisters may be propelled by excessive amount of ROS. To counteract high level of ROS, highly metastatic cells exhibit metabolic dependency on methionine and cysteine (62). Besides, we demonstrate that the metabolic end products of methionine and cysteine act as organic osmolytes (54) to counteract loss of plasma membrane integrity induced by TKI. Collectively, excessive utilization of methionine and cysteine may enable cell undergoing pyroptosis to detoxify ROS and to reduce osmotic imbalance. It will be of potential interest to examine whether these metabolic dependencies exist in macrophage, immune cell type that is known to undergo pyroptosis when exposed to PAMPs and DAMPs.

While increased methionine flux represents a short-term strategy for cells to persist, long term effects can be inevitable. Enhanced flux of methionine to taurine reduces SAH level, which in turn increases cell capacity for methylation of proteins, DNA, and histones. From these, DNA and histones methylation can result in inherited phenotypic changes (63). While gene mutations such as T790M can provide survival benefit in one functional step, stable epigenetic reprograming usually involves multiple genes and several pathways (61). In support, we observed differential methylation pattern of genes regulating metal ion transport, SMADs and type I IFNs. In line with previous studies, epigenetic approaches such as histone deacetylase inhibitors and the bromodomain inhibitor JQ1 ablate emergence of drug tolerant persisters (17, 64). Inhibitors of the histone methyltransferase EZH2 represent another approach to achieve durable response (65, 66).

Finally, the molecular and evolutionary dynamics imposed by cell death in this study may be applicable to a broad range of selection pressures in cancer. For example, poly-anueploid cancer cells remain after chemotherapy contain high amount of lipid droplets (67–69). Chronic exposure of cells to 27-hydroxycholesterol, an abundant circulating cholesterol metabolite, selects for lipid and amino acids scavenging cells (62). Engulfment of extracellular proteins provide a survival tactic in hepatocellular carcinoma during hypoxia (70). Cells emerging from these bottlenecks are highly metastatic and can elicit cancer relapse.

Authors' Disclosures

A. El-Kenawi reports grants from Prostate Cancer Foundation and Urology Care Foundation during the conduct of the study; personal fees from HMP Global; other support from Endocrine society, Federation of American Society for Experimental Biology, and American Urological Association, and from NIH outside the submitted work. No disclosures were reported by the other authors.

Authors' Contributions

A. El-Kenawi: Conceptualization, formal analysis, supervision, funding acquisition, validation, investigation, visualization, methodology, writing–original draft, project administration, writing–review and editing. **A. Berglund:** Formal analysis, visualization, writing–review and editing. **V. Estrella:** Formal analysis, investigation, methodology. **Y. Zhang:** Formal analysis. **M. Liu:** Formal analysis, investigation, methodology. **R.M. Putney:** Formal analysis. **S. Yoder:** Formal analysis, investigation. **J. Johnson:** Formal analysis, investigation. **J. Brown:** Writing–review and editing. **R. Gatenby:** Conceptualization, supervision, funding acquisition, writing–original draft, project administration, writing–review and editing.

Acknowledgments

This work has been supported in part by the Biostatistics & Bioinformatics Shared Resource, Analytic Microscopy Core, Cancer Pharmacokinetics & Pharmacodynamics Core, Molecular Genomics Core and Metabolomics Core Facilities at H. Lee Moffitt Cancer Center & Research Institute, an NCI designated Comprehensive Cancer Center (P30-CA076292). The authors thank Chris Cubitt, Ashley McKee, and Samer Sansil for technical assistance. They thank Drs. Kenneth Pienta, Sarah Amend (John Hopkins University), and Emma Hammarlund (Lund University) for valuable discussions. The authors thank Dr. Kimberly Luddy, Dr. Andriy Marusyk (Cancer Physiology), Marusyk Lab members (Drs. Shirali Xieraili and Daria Miroshnychenko), Ms. Malgorzata Tyczynska, Dr. Virginia Turati, and Dr. Tatiana Miti (Integrated Mathematical Oncology) for providing feedback on the prereviewed version of this article. Illustrations were designed by AE using BioRender.com and Affinity.

This work was supported in part by NIH U54CA193489 (R. Gatenby), NIH/NCI U01CA232382 (R. Gatenby), The 2022 Urology Care Foundation Research Scholar Award Program and the AUA Southeastern Section (A. El-Kenawi), and The 2021 Prostate Cancer Foundation Young Investigator Award (A. El-Kenawi).

The publication costs of this article were defrayed in part by the payment of publication fees. Therefore, and solely to indicate this fact, this article is hereby marked "advertisement" in accordance with 18 USC section 1734.

Note

Supplementary data for this article are available at Cancer Research Online (http://cancerres.aacrjournals.org/).

Received March 31, 2022; revised September 29, 2022; accepted December 2, 2022; published first December 8, 2022.

References

1. Nyati MK, Morgan MA, Feng FY, Lawrence TS. Integration of EGFR inhibitors with radiochemotherapy. Nat Rev Cancer 2006;6:876–85.
2. Blume-Jensen P, Hunter T. Oncogenic kinase signalling. Nature 2001;411: 355–65.
3. Park SY, Kim YM, Pyo H. Gefitinib radiosensitizes non-small cell lung cancer cells through inhibition of ataxia telangiectasia mutated. Mol Cancer 2010;9:222.
4. Girbes T, Citores L, Miguel Ferreras J, Iglesias R. Killing cancer cells by targeting the EGF receptor. Cancer Biol Ther 2008;7:243–4.
5. Arora A, Scholar EM. Role of tyrosine kinase inhibitors in cancer therapy. J Pharmacol Exp Ther 2005;315:971–9.
6. Gan HK, Walker F, Burgess AW, Rigopoulos A, Scott AM, Johns TG, et al. The epidermal growth factor receptor (EGFR) tyrosine kinase inhibitor AG1478 increases the formation of inactive untethered EGFR dimers. Implications for combination therapy with monoclonal antibody 806. J Biol Chem 2007;282: 2840–50.
7. Yuan M, Huang L-L, Chen J-H, Wu J, Xu Q. The emerging treatment landscape of targeted therapy in non-small-cell lung cancer. Signal Transduct Target Ther 2019;4:61.
8. Robert C, Grob JJ, Stroyakovskiy D, Karaszewska B, Hauschild A, Levchenko E, et al. Five-year outcomes with dabrafenib plus trametinib in metastatic melanoma. N Engl J Med 2019;381:626–36.
9. Goel B, Tiwari AK, Pandey RK, Singh AP, Kumar S, Sinha A, et al. Therapeutic approaches for the treatment of head and neck squamous cell carcinoma–an update on clinical trials. Transl Oncol 2022;21:101426.
10. Jonker DJ, O'Callaghan CJ, Karapetis CS, Zalcberg JR, Tu D, Au H-J, et al. Cetuximab for the treatment of colorectal cancer. N Engl J Med 2007;357: 2040–8.
11. Janjigian YY, Maron SB, Chatila WK, Millang B, Chavan SS, Alterman C, et al. First-line pembrolizumab and trastuzumab in HER2-positive oesophageal, gastric, or gastro-oesophageal junction cancer: an open-label, single-arm, phase 2 trial. Lancet Oncol 2020;21:821–31.
12. Yezhelyev MV, Koehl G, Guba M, Brabletz T, Jauch K-W, Ryan A, et al. Inhibition of Src tyrosine kinase as treatment for human pancreatic cancer growing orthotopically in nude mice. Clin Cancer Res 2004;10: 8028–36.
13. Gaut D, Sim MS, Yue Y, Wolf BR, Abarca PA, Carroll JM, et al. Clinical implications of the T790M mutation in disease characteristics and treatment response in patients with epidermal growth factor receptor (EGFR)-mutated non-small-cell lung cancer (NSCLC). Clin Lung Cancer 2018;19:e19–28.
14. Safran HP, Winter K, Ilson DH, Wigle D, DiPetrillo T, Haddock MG, et al. Trastuzumab with trimodality treatment for oesophageal adenocarcinoma with HER2 overexpression (NRG Oncology/RTOG 1010): a multicentre, randomised, phase 3 trial. Lancet Oncol 2022;23:259–69.
15. Qiao Y, Choi JE, Tien JC, Simko SA, Rajendiran T, Vo JN, et al. Autophagy inhibition by targeting PIKfyve potentiates response to immune checkpoint blockade in prostate cancer. Nat Cancer 2021;2:978–93.
16. Whang YE, Armstrong AJ, Rathmell WK, Godley PA, Kim WY, Pruthi RS, et al. A phase II study of lapatinib, a dual EGFR and HER-2 tyrosine kinase inhibitor, in patients with castration-resistant prostate cancer. Urol Oncol 2013;31:82–6.
17. Sharma SV, Lee DY, Li B, Quinlan MP, Takahashi F, Maheswaran S, et al. A chromatin-mediated reversible drug-tolerant state in cancer cell subpopulations. Cell 2010;141:69–80.
18. Hata AN, Niederst MJ, Archibald HL, Gomez-Caraballo M, Siddiqui FM, Mulvey HE, et al. Tumor cells can follow distinct evolutionary paths to become resistant to epidermal growth factor receptor inhibition. Nat Med 2016;22: 262–9.
19. Ramirez M, Rajaram S, Steininger RJ, Osipchuk D, Roth MA, Morinishi LS, et al. Diverse drug-resistance mechanisms can emerge from drug-tolerant cancer persister cells. Nat Commun 2016;7:10690.
20. Hangauer MJ, Viswanathan VS, Ryan MJ, Bole D, Eaton JK, Matov A, et al. Drug-tolerant persister cancer cells are vulnerable to GPX4 inhibition. Nature 2017; 551:247–50.
21. Faber AC, Li D, Song Y, Liang MC, Yeap BY, Bronson RT, et al. Differential induction of apoptosis in HER2 and EGFR addicted cancers following PI3K inhibition. Proc Natl Acad Sci U S A 2009;106:19503–8.
22. Roh H, Pippin J, Drebin JA. Down-regulation of HER2/neu expression induces apoptosis in human cancer cells that overexpress HER2/neu1. Cancer Res 2000; 60:560–5.
23. Lu H, Zhang S, Wu J, Chen M, Cai MC, Fu Y, et al. Molecular targeted therapies elicit concurrent apoptotic and GSDME-dependent pyroptotic tumor cell death. Clin Cancer Res 2018;24:6066–77.
24. Erkes DA, Cai W, Sanchez IM, Purwin TJ, Rogers C, Field CO, et al. Mutant BRAF and MEK inhibitors regulate the tumor immune microenvironment via pyroptosis. Cancer Discov 2020;10:254–69.
25. Deng J, Shimamura T, Perera S, Carlson NE, Cai D, Shapiro GI, et al. Proapoptotic BH3-only BCL-2 family protein BIM connects death signaling from epidermal growth factor receptor inhibition to the mitochondrion. Cancer Res 2007;67:11867–75.
26. Ramos-Junior ES, Morandini AC. Gasdermin: a new player to the inflammasome game. Biomed J 2017;40:313–6.
27. Yu P, Zhang X, Liu N, Tang L, Peng C, Chen X, et al. Pyroptosis: mechanisms and diseases. Signal Transduct Target Ther 2021;6:128.
28. Hu L, Chen M, Chen X, Zhao C, Fang Z, Wang H, et al. Chemotherapy-induced pyroptosis is mediated by BAK/BAX-caspase-3-GSDME pathway and inhibited by 2-bromopalmitate. Cell Death Dis 2020;11:281.
29. Wang Y, Gao W, Shi X, Ding J, Liu W, He H, et al. Chemotherapy drugs induce pyroptosis through caspase-3 cleavage of a gasdermin. Nature 2017;547:99–103.
30. Liu Y-G Chen J-K Zhang Z-T Ma X-J Chen Y-C Du X-M et al. NLRP3 inflammasome activation mediates radiation-induced pyroptosis in bone marrow-derived macrophages. Cell Death Dis 2017;8:e2579.
31. De Santis MC, Porporato PE, Martini M, Morandi A. Signaling pathways regulating redox balance in cancer metabolism. Front Oncol 2018;8:126.
32. Lu J, Shi W, Liang B, C Ca, Wu R, Lin H, et al. Efficient engulfment of necroptotic and pyroptotic cells by nonprofessional and professional phagocytes. Cell Discov 2019;5:39.
33. El-Kenawi A, Dominguez-Viqueira W, Liu M, Awasthi S, Abraham-Miranda J, Keske A, et al. Macrophage-derived cholesterol contributes to therapeutic resistance in prostate cancer. Cancer Res 2021;81:5477–90.
34. Gaidt MM, Hornung V. Pore formation by GSDMD is the effector mechanism of pyroptosis. EMBO J 2016;35:2167–9.
35. Leonetti A, Sharma S, Minari R, Perego P, Giovannetti E, Tiseo M, et al. Resistance mechanisms to osimertinib in EGFR-mutated non-small cell lung cancer. Br J Cancer 2019;121:725–37.
36. Paludan SR, Reinert LS, Hornung V. DNA-stimulated cell death: implications for host defence, inflammatory diseases and cancer. Nat Rev Immunol 2019;19: 141–53.
37. Smith ER, Capo-chichi CD, Xu X-X. Defective nuclear lamina in aneuploidy and carcinogenesis. Front Oncol 2018;8:529.
38. Nmezi B, Xu J, Fu R, Armiger TJ, Rodriguez-Bey G, Powell JS, et al. Concentric organization of A- and B-type lamins predicts their distinct roles in the spatial organization and stability of the nuclear lamina. Proc Natl Acad Sci U S A 2019; 116:4307–15.
39. Gaillard H, García-Muse T, Aguilera A. Replication stress and cancer. Nat Rev Cancer 2015;15:276–89.
40. Brzostek-Racine S, Gordon C, Van Scoy S, Reich NC. The DNA damage response induces IFN. J Immunol 2011;187:5336–45.
41. Negishi H, Taniguchi T, Yanai H. The interferon (IFN) class of cytokines and the IFN regulatory factor (IRF) transcription factor family. Cold Spring Harb Perspect Biol 2018;10:a028423.
42. Muhammad JS, Jayakumar MN, Elemam NM, Venkatachalam T, Raju TK, Hamoudi RA, et al. Gasdermin D hypermethylation inhibits pyroptosis and LPS-induced IL-1beta release from NK92 cells. Immunotargets Ther 2019;8:29–41.
43. Banerjee I, Behl B, Mendonca M, Shrivastava G, Russo AJ, Menoret A, et al. Gasdermin D restrains type I interferon response to cytosolic DNA by disrupting ionic homeostasis. Immunity 2018;49:413–26.
44. Humphries F, Shmuel-Galia L, Ketelut-Carneiro N, Li S, Wang B, Nemmara VV, et al. Succination inactivates gasdermin D and blocks pyroptosis. Science 2020; 369:1633–7.
45. Lachkar F, Ferré P, Foufelle F, Papaioannou A. Dihydroceramides: their emerging physiological roles and functions in cancer and metabolic diseases. Am J Physiol Endocrinol Metab 2021;320:E122–E30.
46. Viswanathan VS, Ryan MJ, Dhruv HD, Gill S, Eichhoff OM, Seashore-Ludlow B, et al. Dependency of a therapy-resistant state of cancer cells on a lipid peroxidase pathway. Nature 2017;547:453–7.
47. Xu C, Zhang L, Wang D, Jiang S, Cao D, Zhao Z, et al. Lipidomics reveals that sustained SREBP-1-dependent lipogenesis is a key mediator of gefitinib-acquired resistance in EGFR-mutant lung cancer. Cell Death Discov 2021;7:353.

48. Ali A, Levantini E, Teo JT, Goggi J, Clohessy JG, Wu CS, et al. Fatty acid synthase mediates EGFR palmitoylation in EGFR mutated non-small cell lung cancer. EMBO Mol Med 2018;10:e8313.
49. Mitchell RW, On NH, Del Bigio MR, Miller DW, Hatch GM. Fatty acid transport protein expression in human brain and potential role in fatty acid transport across human brain microvessel endothelial cells. J Neurochem 2011;117:735–46.
50. Gimeno RE, Ortegon AM, Patel S, Punreddy S, Ge P, Sun Y, et al. Characterization of a heart-specific fatty acid transport protein. J Biol Chem 2003;278:16039–44.
51. Oren Y, Tsabar M, Cuoco MS, Amir-Zilberstein L, Cabanos HF, Hutter JC, et al. Cycling cancer persister cells arise from lineages with distinct programs. Nature 2021;596:576–82.
52. Zhang F, Warskulat U, Wettstein M, Häussinger D. Identification of betaine as an osmolyte in rat liver macrophages (Kupffer cells). Gastroenterology 1996;110:1543–52.
53. Burg MB, Ferraris JD. Intracellular organic osmolytes: function and regulation. J Biol Chem 2008;283:7309–13.
54. Li G, Olson JE. Purinergic activation of anion conductance and osmolyte efflux in cultured rat hippocampal neurons. Am J Physiol Cell Physiol 2008;295:C1550–60.
55. Sun Q, Hu Y, Gu Y, Huang J, He J, Luo L, et al. Deciphering the regulatory and catalytic mechanisms of an unusual SAM-dependent enzyme. Signal Transduct Target Ther 2019;4:17.
56. Summersgill H, England H, Lopez-Castejon G, Lawrence CB, Luheshi NM, Pahle J, et al. Zinc depletion regulates the processing and secretion of IL-1β. Cell Death Dis 2014;5:e1040.
57. Gao H, Zhao L, Wang H, Xie E, Wang X, Wu Q, et al. Metal transporter Slc39a10 regulates susceptibility to inflammatory stimuli by controlling macrophage survival. Proc Natl Acad Sci U S A 2017;114:12940–5.
58. Xia X, Wang X, Cheng Z, Qin W, Lei L, Jiang J, et al. The role of pyroptosis in cancer: pro-cancer or pro-"host"? Cell Death Dis 2019;10:650.
59. Wang L, Qin X, Liang J, Ge P. Induction of pyroptosis: a promising strategy for cancer treatment. Front Oncol 2021;11:635774.
60. Yatabe Y, Tavaré S, Shibata D. Investigating stem cells in human colon by using methylation patterns. Proc Natl Acad Sci U S A 2001;98:10839–44.
61. Brown R, Curry E, Magnani L, Wilhelm-Benartzi CS, Borley J. Poised epigenetic states and acquired drug resistance in cancer. Nat Rev Cancer 2014;14:747–53.
62. Liu W, Chakraborty B, Safi R, Kazmin D, Chang CY, McDonnell DP, et al. Dysregulated cholesterol homeostasis results in resistance to ferroptosis increasing tumorigenicity and metastasis in cancer. Nat Commun 2021;12:5103.
63. Easwaran H, Tsai H-C, Baylin Stephen B, Cancer epigenetics: tumor heterogeneity, plasticity of stem-like states, and drug resistance. Mol Cell 2014;54:716–27.
64. Knoechel B, Roderick JE, Williamson KE, Zhu J, Lohr JG, Cotton MJ, et al. An epigenetic mechanism of resistance to targeted therapy in T cell acute lymphoblastic leukemia. Nat Genet 2014;46:364–70.
65. Liau BB, Sievers C, Donohue LK, Gillespie SM, Flavahan WA, Miller TE, et al. Adaptive chromatin remodeling drives glioblastoma stem cell plasticity and drug tolerance. Cell stem cell 2017;20:233–46.
66. Pham V, Pitti R, Tindell CA, Cheung TK, Masselot A, Stephan J-P, et al. Proteomic analyses identify a novel role for EZH2 in the initiation of cancer cell drug tolerance. J Proteome Res 2020;19:1533–47.
67. Pienta KJ, Hammarlund EU, Brown JS, Amend SR, Axelrod RM. Cancer recurrence and lethality are enabled by enhanced survival and reversible cell cycle arrest of polyaneuploid cells. Proc Natl Acad Sci U S A 2021;118:e2020838118.
68. Kuczler MD, Olseen AM, Pienta KJ, Amend SR. ROS-induced cell cycle arrest as a mechanism of resistance in polyaneuploid cancer cells (PACCs). Prog Biophys Mol Biol 2021;165:3–7.
69. Pienta KJ, Hammarlund EU, Axelrod R, Brown JS, Amend SR. Poly-aneuploid cancer cells promote evolvability, generating lethal cancer. Evol Appl 2020;13:1626–34.
70. Zhang MS, Cui JD, Lee D, Yuen VW-H, Chiu DK-C, Goh CC, et al. Hypoxia-induced macropinocytosis represents a metabolic route for liver cancer. Nat Commun 2022;13:954.